

High sensitivity dual core photonic crystal fiber sensor for simultaneous detection of two samples

Pibin Bing(邴丕彬), Guifang Wu(武桂芳), Qing Liu(刘庆), Zhongyang Li(李忠洋),Lian Tan(谭联), Hongtao Zhang(张红涛), and Jianquan Yao(姚建铨)

Citation: Chin. Phys. B, 2022, 31 (**8**): 084208. DOI: 10.1088/1674-1056/ac4a68
Journal homepage: http://cpb.iphy.ac.cn; http://iopscience.iop.org/cpb

What follows is a list of articles you may be interested in

Design of a polarization splitter for an ultra-broadband dual-core photonic crystal fiber

Yongtao Li(李永涛), Jiesong Deng(邓洁松), Zhen Yang(阳圳), Hui Zou(邹辉), and Yuzhou Ma(马玉周)
Chin. Phys. B, 2022, 31 (**5**): 054215. DOI: 10.1088/1674-1056/ac3a63

Generation of mid-infrared supercontinuum by designing circular photonic crystal fiber

Ying Huang(黄颖), Hua Yang(杨华), and Yucheng Mao(毛雨澄)
Chin. Phys. B, 2022, 31 (**5**): 054211. DOI: 10.1088/1674-1056/ac272c

High sensitivity plasmonic temperature sensor based on a side-polished photonic crystal fiber

Zhigang Gao(高治刚), Xili Jing(井西利), Yundong Liu(刘云东), Hailiang Chen(陈海良), and Shuguang Li(李曙光)
Chin. Phys. B, 2022, 31 (**2**): 024207. DOI: 10.1088/1674-1056/ac0a63

Mid-infrared supercontinuum and optical frequency comb generations in a multimode tellurite photonic crystal fiber

Xu Han(韩旭), Ying Han(韩颖), Chao Mei(梅超), Jing-Zhao Guan(管景昭), Yan Wang(王彦), Lin Gong(龚琳), Jin-Hui Yuan(苑金辉), and Chong-Xiu Yu(余重秀)
Chin. Phys. B, 2021, 30 (**9**): 094207. DOI: 10.1088/1674-1056/abf10f

Generation of wideband tunable femtosecond laser based on nonlinear propagation of power-scaled mode-locked femtosecond laser pulses in photonic crystal fiber

Zhiguo Lv(吕志国) and Hao Teng(滕浩)
Chin. Phys. B, 2021, 30 (**4**): 044209. DOI: 10.1088/1674-1056/abe231

High sensitivity dual core photonic crystal fiber sensor for simultaneous detection of two samples

Pibin Bing(邴丕彬)[1,†], Guifang Wu(武桂芳)[1], Qing Liu(刘庆)[1], Zhongyang Li(李忠洋)[1], Lian Tan(谭联)[1], Hongtao Zhang(张红涛)[1], and Jianquan Yao(姚建铨)[1,2]

[1] *College of Electric Power, North China University of Water Resources and Electric Power, Zhengzhou* 450045, *China*
[2] *College of Precision Instrument and Opto-Electronics Engineering, Institute of Laser and Opto-Electronics, Tianjin University, Tianjin* 300072, *China*

(Received 7 November 2021; revised manuscript received 27 December 2021; accepted manuscript online 12 January 2022)

The optical control ability of photonic crystal fiber (PCF) is a distinctive property suitable for improving sensing and plasma performance. This article proposes a dual-core D-channel PCF sensor that can detect two samples simultaneously, which effectively solves the problems of coating difficulty and low wavelength sensitivity. The PCF has four layers of air holes, which dramatically reduces the optical fiber loss and is more conducive to the application of sensors in actual production. In addition, by introducing dual cores on the upper and lower sides of the central air hole, reducing the spacing between the core and the gold nanolayer, a stronger evanescent field can be generated in the cladding air hole. The optical fiber sensor can detect the refractive index of two samples simultaneously with a maximum sensitivity of 21300 nm/RIU. To the best of our knowledge, the sensitivity achieved in this work is the highest sensitivity with the dual sample synchronous detection sensors. The detection range of the refraction index is 1.35–1.41, and the resolution of the sensor is 4.695×10^{-6}. Overall, the sensor will be suitable for medical detection, organic chemical sensing, analyte detection, and other fields.

Keywords: photonic crystal fiber, surface plasma resonance, sensor

PACS: 42.81.Pa, 07.07.Df, 71.45.Gm **DOI:** 10.1088/1674-1056/ac4a68

1. Introduction

Optical fiber sensors have attracted widespread attention because of their small size, strong anti-electromagnetic interference ability, high sensitivity, and suitability for harsh environments. In modern times, surface plasma resonance (SPR) technology has the peculiarities of analytical biosensors because it provides label-free and real-time monitoring.[1–3] The PCF based on SPR technology is a crucial platform for designing biosensors because of its attractive characteristics such as flexible and controllable dispersion, high sensitivity, and high birefringence effect. With the rapid development of sensors, the designs of biosensors based on SPR-PCF technology have received extensive attention from professionals in the fields of environmental testing, water quality detection, medical testing and so on.[4–6] For instance, a D-type SPR-PCF sensor with a maximal sensitivity of 46000 nm/RIU was reported by Rifat *et al.* in 2017.[7] Kuar and Singh proposed a PCF biosensor based on TiN metal coating. TiN has the advantages of chemical stability and high conductivity, so it can be used as plasma-material. The high wavelength sensitivity of 10000 nm/RIU has been achieved in the refractive index range of 1.385–1.40.[8] Moreover, a variety of multi-core optical fiber sensors including dual-core sensors are also proposed.[9–13] For example, Paul reported a dual-core sensor that can achieve a sensitivity of up to 9000 nm/RIU.[14] With the rapid development of clinical diagnosis, drug screening and environmental monitoring, the traditional single parameter SPR sensor cannot satisfy the demands of multi-parameter detection applications. Furthermore, multi-channel and high-throughput sensors have attracted extensive attention of researchers. In the past decade, multi-channel SPR sensors have been a research hotspot in the sensing field.[15,16] In 2016, Azzam presented a multi-channel PCF sensor with sensitivity up to 2400 nm/RIU which has four microfluid channels with gold coating and analyzed four different propagating modes.[17] Yasli reported a multi-channel detection sensor, a metal-coated medium composed of silver and gold, which can obtain sensitivities of 3083 nm/RIU and 2500 nm/RIU in 2020.[18] In the same year, a dual-sample synchronous detection PCF sensor was proposed by Bing *et al.*, with dual-channel wavelength sensitivity of 11600 nm/RIU and 10600 nm/RIU, respectively, and the refractive index detection range is 1.33–1.40.[19] The dual channel PCF sensor can detect a single sample or two samples synchronously. Compared with the single channel PCF sensor, it reduces the steps of emptying, filling and multiple cleaning of the samples. In practical application, the dual channel PCF sensor can also detect two different parameters of the same sample by covering different sensing media in different channels. For example, the temperature and pH of the sample can be measured simultaneously. A thermo optic material can be coated on the metal film surface of channel A for temperature detection. A layer of pH sol gel is deposited on the metal film surface of

[†]Corresponding author. E-mail: bing463233@163.com

© 2022 Chinese Physical Society and IOP Publishing Ltd

channel B to detect the change of pH.[15,20] In short, the dual channel PCF sensor can detect two samples or two parameters at the same time. This paper mainly studies the performance of the sensor when two samples are detected synchronously. Dual-channel PCF sensors are expected to be developed in the fields of medical detection, organic chemical sensing and bio-engineering detection.

This article proposes a dual-core D-channel PCF sensor that can detect two samples simultaneously, which effectively solves the problems of coating difficulty and low wavelength sensitivity. Through spectral sensitivity analysis, the maximum sensitivity of the dual-channel sensor is 21300 nm/RIU, which achieves the highest sensitivity of the dual-sample synchronous detection sensor.

2. Theory and method

The structure of the high-sensitivity dual-core PCF sensor is presented in Fig. 1. The outermost layer increases a circular perfect matching layer (PML) with a thickness of 3 μm to absorb radiation power. Four layers of small air holes are arranged radially from the inside to the outside of the center of the substrate, with the first layer of small air holes closest to the center of the substrate and arranged in an outward order. To form the two cores C_1 and C_2, the two small air holes in the third layer of air holes are omitted. The D-shaped air hole channel A is provided above the central air hole of the optical fiber, and a D-shaped air hole channel B is arranged below. A gold nanolayer of equal thickness is deposited on the plane of channel A and channel B. The diameter of all the small air holes of the optical fiber is $d_1 = 0.4\Lambda$ and the spacing between adjacent small air holes is $\Lambda = 2$ μm. The simultaneous measurement of the refractive indexes of both samples is achieved by filling channels A and B with two samples with refractive indexes of N_A and N_B, respectively. The diameters of channels A and B are $d_D = 5.29\Lambda$. The distance between the D-shaped channel and the central air hole is $H = 6.2$ μm. Gold is selected as plasma-material because it has good stability and strong chemical inertness. Gold nanolayers with a thickness of $t_g = 40$ nm are plated on the polished planes of both the A and B channels. SiO_2 is chosen as the background material, and when the wavelength changes, the specific refractive index of the SiO_2 can be obtained by the Sellmeier equation[21]

$$n^2_{SiO_2}(\lambda) = 1 + \frac{A_1\lambda^2}{\lambda^2 - B_1} + \frac{A_2\lambda^2}{\lambda^2 - B_2} + \frac{A_3\lambda^2}{\lambda^2 - B_3}, \quad (1)$$

where λ is the wavelength of the incident light, A_1, A_2, and A_3 are respectively equal to 0.6961663, 0.4079426, 0.8974794, B_1, B_2, and B_3 are respectively equal to $4.67914826 \times 10^{-3}$ μm^2, $1.35120631 \times 10^{-2}$ μm^2, 97.9340025 μm^2, and the more accurate value of the dielectric constant of gold can be expressed by the Drude model.[22]

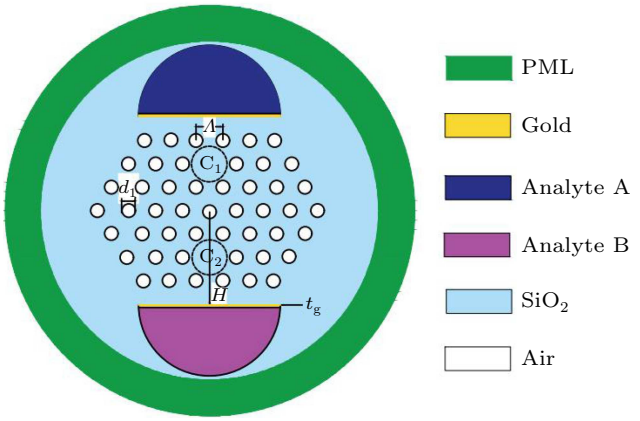


Fig. 1. Optical fiber structure diagram.

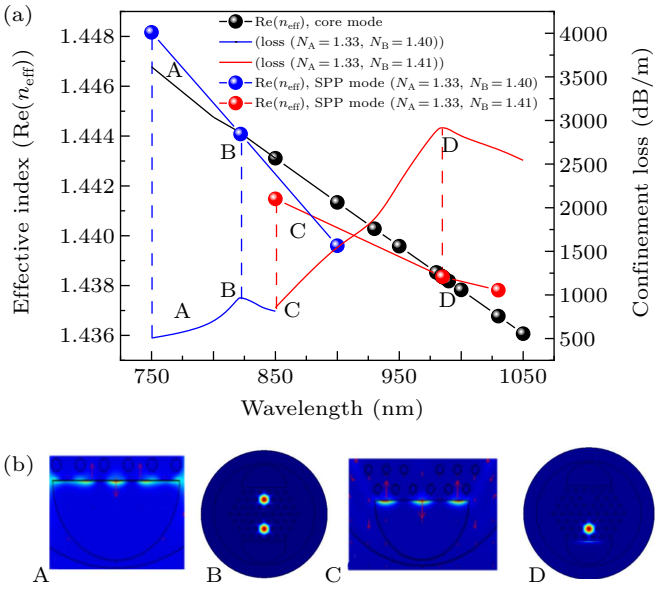


Fig. 2. (a) The loss spectra of core mode and SPP mode at different wavelengths. (b) The four electric field distribution maps correspond to points A, B, C, and D, respectively.

Theoretically, to achieve the phase matching between the SPP mode and the core mode, the real part of the refractive indexes ($\mathrm{Re}(n_{\mathrm{eff}})$) of the two modes must be equal. Figure 2 describes $\mathrm{Re}(n_{\mathrm{eff}})$ and loss spectrum of the two modes when $N_A = 1.33$, $N_B = 1.40$, and $N_A = 1.33$, $N_B = 1.41$, and the electric field distribution at points A, B, C, and D. Point A in Fig. 2(a) indicates that when $N_A = 1.33$, $N_B = 1.40$, $\lambda = 750$ nm, the value of $\mathrm{Re}(n_{\mathrm{eff}})$ in SPP mode is greater than the value of $\mathrm{Re}(n_{\mathrm{eff}})$ in core mode, and the fiber core energy is continuously transferred to the metal nanolayer, and the loss slowly increases. When $\lambda = 822$ nm, the loss reaches the maximum, that is point B in Fig. 2(a), and the $\mathrm{Re}(n_{\mathrm{eff}})$ value of the SPP mode and the $\mathrm{Re}(n_{\mathrm{eff}})$ value of the core mode will be equal, and a phase match occurs between them. Most of the fiber core energy is absorbed by the gold nanolayer. When the incident wavelength continuously increases, $\mathrm{Re}(n_{\mathrm{eff}})$ in SPP

mode is smaller than Re(n_{eff}) in core mode. At this time, the SPR effect continues to weaken, and energy begins to transfer from the gold nanolayer to the core, resulting in the SPR effect, and the loss continues to decrease. From the electric field distribution diagram of point D in Fig. 2(b), point D is also a phase-matching point, and the entire optical field is enclosed in the core. Besides, plasma can be observed on the metal coating of polished plane of the D-channel.

3. Results and discussion

The amplitude detection method adopts light incident at a single wavelength, and samples with different refractive indexes have various losses at this wavelength. The corresponding samples can be detected by measuring the transmitted light power of the sensor. The confinement loss is able to be accurately calculated by the following formula:[23]

$$\alpha_{\text{loss}}\ (\text{dB/m}) = 40\pi \frac{\text{Im}[n_{\text{eff}}]}{\ln(10)\lambda}, \tag{2}$$

where the refractive index is expressed in n_{eff}, and λ is the wavelength of incident light.[24] When samples with refractive indexes of N_{A} and N_{B} are respectively filled into channel A and channel B, the SPR effect will occur on the gold nanolayer in channels A and B. Therefore, both resonance peaks appear on the spectrum by the simulation experiments. As can be seen from Fig. 3(a), the refractive index $N_{\text{A}} = 1.33$ of sample in channel A remains unchanged, and the resonance wavelength always remains around 591 nm when the loss curve of channel A reaches its peak. Therefore, the wavelength sensitivity of sample B at different refractive indexes can be obtained according to the offset of the resonant peak of channel B.

Similarly, the refractive index N_{A} of the sample in channel A is 1.39, and the refractive index N_{B} varies within the range of 1.35–1.41. The peak value of the loss curve in channel A always varies around 647 nm. As the difference value between N_{A} and N_{B} increases, the resonance wavelength spacing between A and B also increases, and the ability to distinguish the two samples is enhanced. Therefore, the channels A and B can detect the refractive index simultaneously, and the two channels are independent of each other.

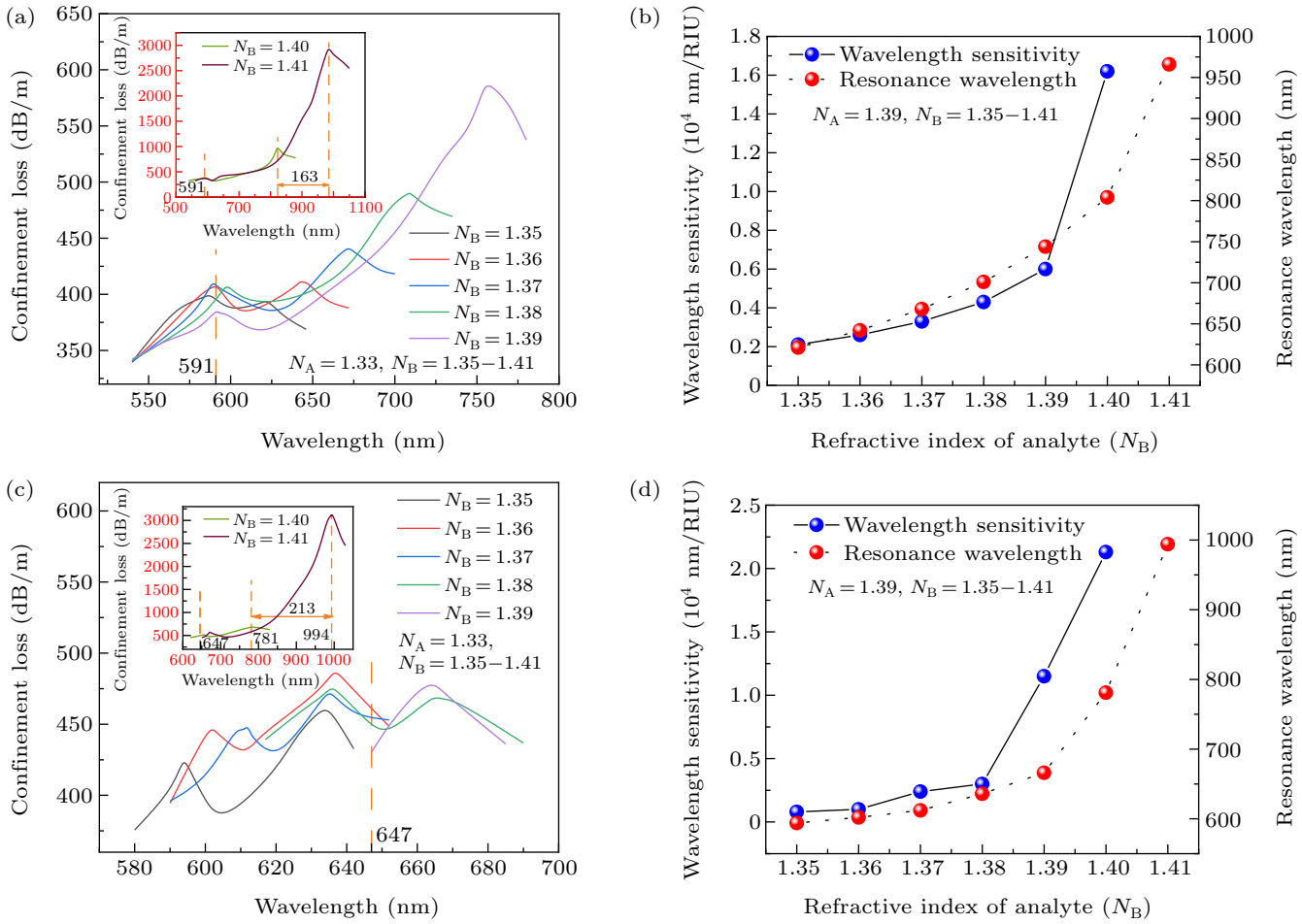


Fig. 3. (a) When $N_{\text{A}} = 1.33$, $N_{\text{B}} = 1.35$–1.41, the resonance peak spectrum of the sensor under different refractive index N_{B}. (b) When refractive index $N_{\text{B}} = 1.35$ increases to $N_{\text{B}} = 1.41$, the sensitivity and resonance wavelength change with the change of N_{B}. (c) When $N_{\text{A}} = 1.39$, $N_{\text{B}} = 1.35$–1.41, the resonance peak spectrum of the sensor under different refractive index N_{B}. (d) When refractive index $N_{\text{B}} = 1.35$ increases to $N_{\text{B}} = 1.41$, the sensitivity and resonance wavelength change with the change of N_{B}.

Sensitivity and minimum resolution are both indicators to measure whether the refractive index sensor is excellent, and the wavelength sensitivity in this article is measured by the spectral detection method, and the formula is as follows:[25]

$$S_\lambda\ (\mathrm{nm/RIU}) = \Delta\lambda_{\mathrm{peak}}/\Delta n, \tag{3}$$

where $\Delta\lambda_{\mathrm{peak}}$ refers to the shift of the resonance peak on the spectrum, and the change in refractive index is represented by Δn. Figure 3(b) demonstrates that the sensor's sensitivity also changes when the N_{B} value increases from 1.35 to 1.41. It is clear from the loss spectrum that 621 nm, 643 nm, 672 nm, 709 nm, 757 nm, 822 nm, and 985 nm are the resonance wavelengths corresponding to different N_{B} refractive indexes. The proposed sensor demonstrates resonant wavelength shifts of 22 nm, 29 nm, 37 nm, 48 nm, 65 nm, and 163 nm, and corresponding refractive indexes are 1.35, 1.36, 1.37, 1.38, 1.39, and 1.40, respectively. When the refractive index $N_{\mathrm{A}} = 1.33$, $N_{\mathrm{B}} = 1.35$–1.41, according to Eq. (3), the sensor can obtain the upmost wavelength sensitivity of 16300 nm/RIU. Figure 3(d) demonstrates that when $N_{\mathrm{A}} = 1.39$ and the value of N_{B} increases from 1.35 to 1.41, the sensor's sensitivity will also change. It can be concluded from the loss spectrum that 594 nm, 602 nm, 612 nm, 636 nm, 666 nm, 781 nm, and 994 nm are the resonance wavelengths corresponding to different N_{B} refractive indexes. Furthermore, we must note that channels A and B are symmetric and they have equivalent effects. When the refractive index $N_{\mathrm{A}} = 1.39$, N_{B} changes in the range of 1.35–1.41, the sensitivity value is the same as that of $N_{\mathrm{B}} = 1.39$ and N_{A} changes in the range of 1.35–1.41, which can reach 21300 nm/RIU.

The resolution of sensor refers to the most minor change in the measurement parameters of the sample that the system can detect. The smaller the value of the minimum resolution, the better sensor's performance, and it is customary to use the following formula to express resolution:[26]

$$R\ (\mathrm{RIU}) = \Delta\lambda_{\mathrm{min}}\Delta n/\Delta\lambda_{\mathrm{res}} = \Delta\lambda_{\mathrm{min}}/S_\lambda, \tag{4}$$

where Δn and $\Delta\lambda_{\mathrm{min}}$ are the change in refractive index and the minimum resolution of the spectrum respectively. According to the Eq. (4), it is clear that the greater the resonance wavelength shift is, the lower the sensor resolution is, hence, a small change in the refractive index of the sample can be detected accurately. Assuming that $\Delta\lambda_{\mathrm{min}} = 0.1$ nm is the minimum resolution unit of the spectrometer, the resolution of the sensor is 4.695×10^{-6}, which indicates that the sensor can detect small refractive index changes of the order of 10^{-6}, and this result is better than the result reported in Refs. [27–29]. In summary, since the wavelength sensitivity and resolution are better than the same kind of sensor for dual sample synchronous detection, it will become an ideal sensor for sample detection such as medical testing, organic chemical sensing, and biological sensing.

This paper studies the effect of structural parameters (gold nanolayer thickness t_{g}, central air hole radius r, vertical distance H) on the sensitivity and loss of the sensor when the refractive index $N_{\mathrm{A}} = 1.33$, $N_{\mathrm{B}} = 1.37$. Different parameters also affect wavelength sensitivity, and the results are shown in the figures. After many simulation experiments, we obtain the best parameters for the proposed fiber structure.

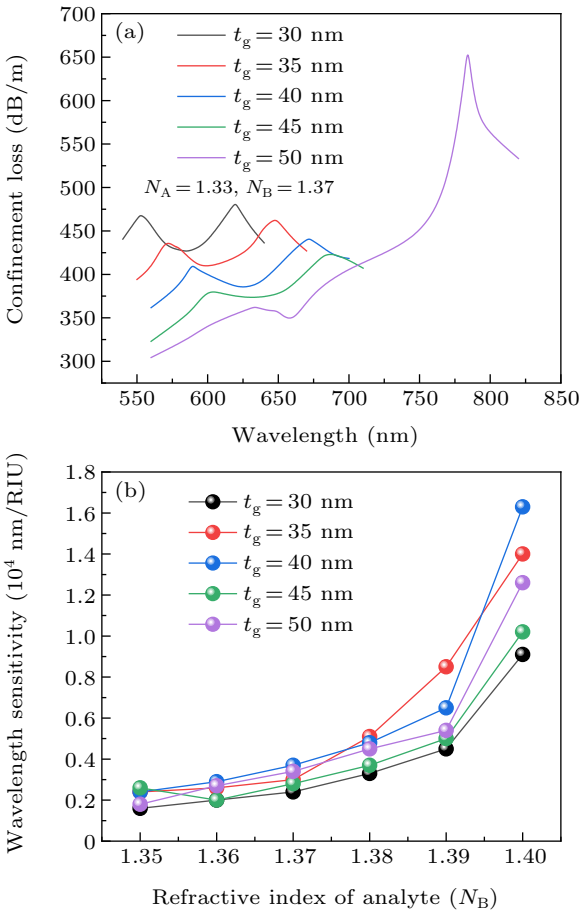


Fig. 4. (a) The loss spectrum of sensor with different thickness of gold nanolayer. (b) The change of wavelength sensitivity with different gold nanolayer thicknesses.

Gold has good stability and strong chemical inertness, so it has good application value in SPR. Therefore, the optical fiber chooses gold as the coating material to produce the SPR effect, and the position of the resonant peak and the wavelength sensitivity will change with the different thickness of gold nanolayer. If the gold nanolayer is excessively thick, it will weaken the penetration of the evanescent field, thereby reducing the sensitivity and confinement loss. If the gold nanolayer becomes thin, the plasma wave will be damped and strongly suppressed. Figure 4(a) demonstrates the core mode loss spectrum at different gold nanolayer thicknesses. When the thickness of the gold nanolayer increases from 30 nm to 50 nm, the loss peak gradually redshifts. As shown in the Fig. 4(b), the sensitivity increases nonlinearly when the gold

nanolayer thickness t_g remains unchanged and the refractive index N_B increases. When $t_g = 40$ nm, the maximum wavelength sensitivity of the sensor is 16300 nm/RIU.

This paper anatomizes the effect of the vertical distance H from channel D to the central air hole on wavelength sensitivity and confinement loss, and the change of confinement loss is shown in the Fig. 5(a). When $H = 6.0$ μm, the peak loss is the maximum value of 652.1 dB/m. When $H = 6.4$ μm, the peak loss is the minimum value of 303 dB/m. Figure 5(a) shows that the loss intensity continues to decrease as the vertical distance H increases. Due to the large vertical distance H, the energy leaking into the gold nanolayer is reduced, thus weakening the resonance strength. Figure 5(b) demonstrates the effect of different vertical distances on wavelength sensitivity. When H is constant, the sensitivity value increases with the increase in the refractive index. Due to the offset of resonance wavelength $\Delta\lambda_{peak}$ does not increase linearly with the increase of vertical distance, the wavelength sensitivity does not increase linearly, but we can still obtain an optimal value of vertical distance H by simulation. When $H = 6.2$ μm, the wavelength sensitivity of channel B reaches the maximum. Therefore, the sensor chooses the vertical distance $H = 6.2$ μm as the optimal parameter.

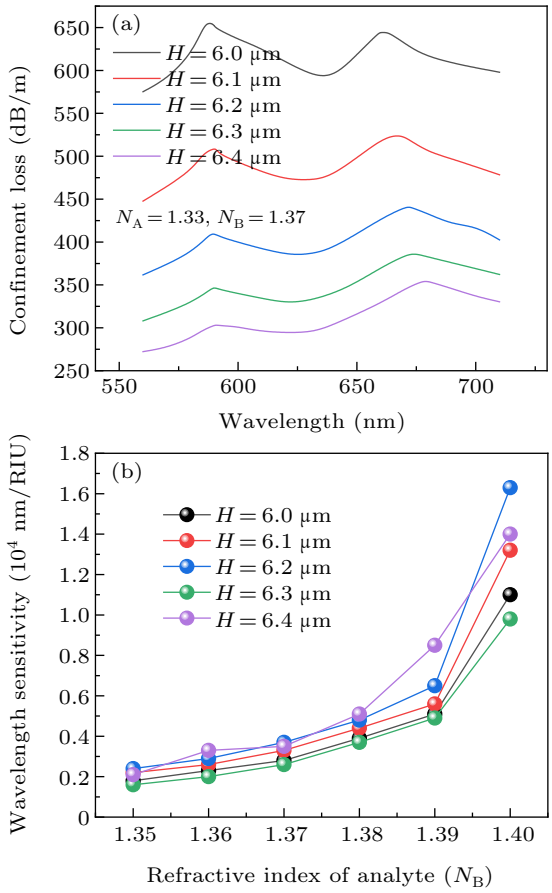


Fig. 5. (a) The confinement loss varies with the vertical distance H. (b) The vertical distance H varies with wavelength sensitivity.

Figure 6(a) displays the loss curves of the core mode when the radius r of central air hole changes. The fiber loss increases with the increase of radius r. The reason is that the larger central air hole is more conducive to concentrating the mode field energy of the core, thus effectively improving the coupling strength between the core mode and the SPP mode, and increasing the peak loss. As seen from Fig. 6(b), the changes of the central air hole radius have little effect on the sensitivity. The wavelength sensitivity at the radius of the central air hole $r = 0.4$ μm is higher than that at the radius of the central air hole $r = 1.0$ μm. In short, the sensor has the utmost performance when the radius of the central air hole is $r = 0.4$ μm.

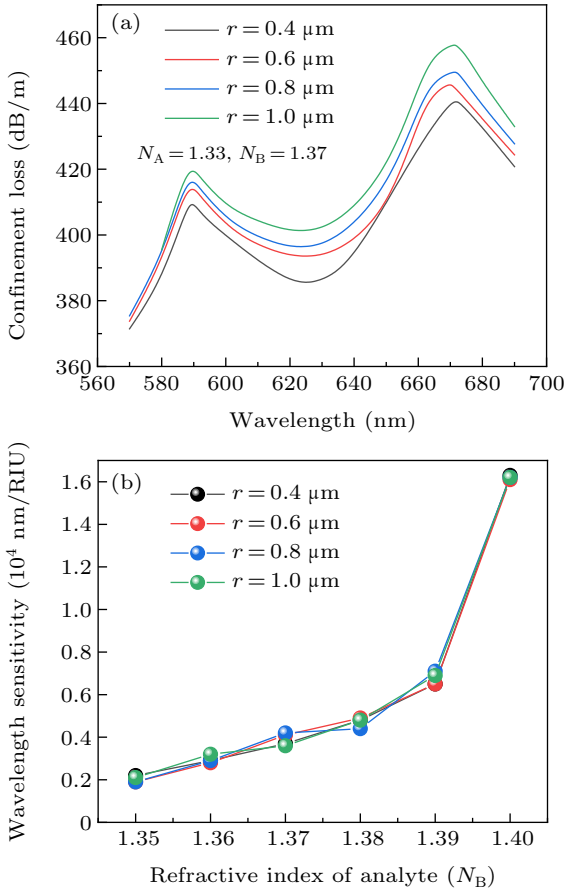


Fig. 6. (a) The loss spectrum of sensor with different central air hole radius. (b) The change of wavelength sensitivity as the radius of the central air hole increases.

Since the fiber core of the single-core PCF sensor is far away from the sample channel, the evanescent field faces a longer transmission distance, and more free electrons in the gold nanolayer are required to form the SPR effect. The evanescent field may disappear before reaching the metal surface, and the free electrons are not effectively excited.[30–32] This paper proposes a dual-core PCF sensor that can effectively solve the above problems. A fiber core is arranged on the upper and lower sides of the central air hole, respectively. It not only guarantees the high-quality transmission of incoming energy, but the evanescent field is also closer to the metal surface of the sample channel. Figure 7 is a comparison diagram of the wavelength sensitivity values of single-core PCF

and dual-core PCF, the maximum wavelength sensitivity of single-core PCF is 12300 nm/RIU, while dual-core PCF is up to 16300 nm/RIU. Besides, the dual-core PCF proposed in this paper can also manufacture polarization modulators or polarization couplers based on the coupling effect between the two cores, which is more widely used than single-core PCF.

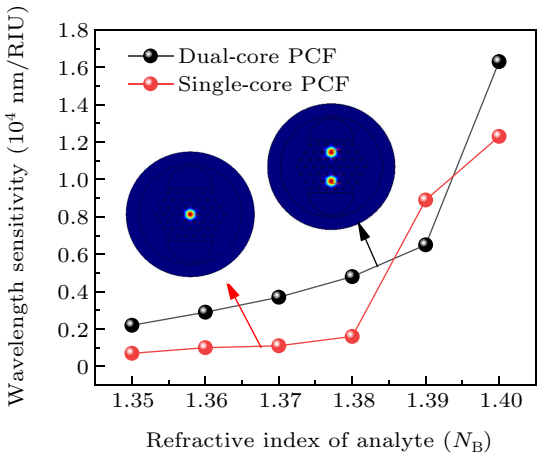


Fig. 7. Wavelength sensitivity of single-core PCF and dual-core PCF when $N_B = 1.35$–1.40.

The dual channel PCF sensor can detect a single sample or two samples synchronously. Compared with the single channel PCF sensor, it reduces the steps of emptying, filling and multiple cleaning of the samples. Figure 8 shows the influences of channel B filled and unfilled with samples on the resonance wavelength. The blue curve shows the loss change in the sample-filled A and B channels with $N_A = 1.33$ and $N_B = 1.36$. The orange curve shows the change of optical fiber loss when D-type large air channel A is filled with sample with refractive index $N_A = 1.33$ and channel B is not filled with sample. Because the gold film thickness of channel A and the vertical distance from the fiber core do not change, the intensity of optical coupling to the surface of gold and the sample does not change significantly, and the resonance wavelength remains at 591 nm. Therefore, when we detect a single sample, only one D-shaped channel needs to be coated, which reduces the complexity of coating operation, upgrades the detection efficiency, and makes the application range of the sensor more extensive.

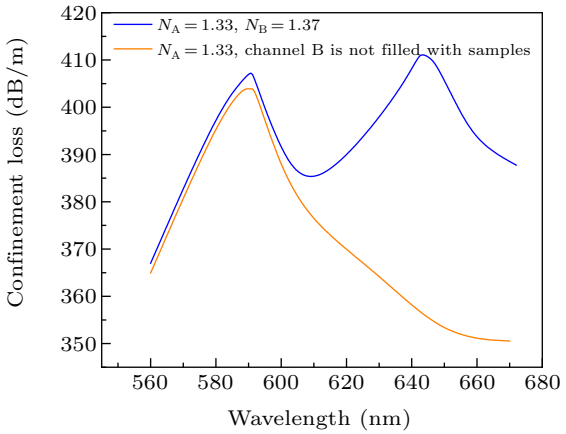


Fig. 8. The influences of channel B filled and unfilled with samples on resonance wavelength.

The critical performance of this sensor is shown in Table 1. The performance of the sensor provided is better than the previously reported SPR-PCF sensor. Currently, our reported sensor has higher wavelength sensitivity than that of similar dual-sample synchronous detection of PCF sensors. All in all, the sensor has outstanding performance in terms of wavelength sensitivity, detection range and resolution, as shown in the table.

Table 1. The important performance of the proposed sensor is compared with other similar sensors.

Ref.	Detection range	Sensitivity (nm/RIU)	Resolution (RIU)	Detection type
[9]	1.42–1.46	15000	6.67×10^{6}	single-sample test
[10]	1.33–1.43	3580	2.79×10^{-6}	single-sample test
[11]	1.33–1.37	4200	2.38×10^{-6}	single-sample test
[17]	1.33–1.34	2200 and 2400	4.55×10^{-5} and 4.17×10^{-5}	dual-sample test
[18]	1.33–1.366	2500 and 3083	4.00×10^{-5} and 3.24×10^{-5}	dual-sample test
[19]	1.33–1.40	10600 and 11600	9.43×10^{-6} and 8.62×10^{-6}	dual-sample test
This work	1.35–1.41	16300 and 21300	6.13×10^{-6} and 4.67×10^{-6}	dual-sample test

In the specific manufacturing process of the PCF sensor, two solid glass rods are selected as two fiber cores based on the number of fiber cores and cladding layers of D-shaped PCF. During stretching, the inert gas is introduced into the capillary glass tube to adjust its internal air pressure, and the two core D-shaped PCF is obtained by controlling the tensile velocity. Flat polishing is performed along the D-plane side to dip the fiber directly into the sample or drop the sample onto the D-polished side of the fiber.[7,19] Magnetron sputtering technology is used to reduce the coating difficulty and avoid microfluidic filling. This method is easy to implement and it not only ensures uniformity of the coating but also reduces the scrapping rate of D-type PCFs.

4. Conclusion

This article proposes a dual-core D-channel PCF sensor that can detect two samples simultaneously, which effectively solves the problems of coating difficulty and low wavelength sensitivity. The dual-core PCF has demonstrated outstanding

performance in various application fields, such as polarizing beam splitters, polarizing filters and sensors for detecting refractive index. In practical application, the dual channel PCF sensor can detect two different samples and two different parameters of the same sample, which is realized by covering different sensing media in different channels. Furthermore, the influence of parameters such as the vertical distance H, the central air hole radius r and thickness of the gold nanolayer t_g on the sensor performance are also analyzed to obtain the best parameters of the proposed structure. The optical fiber sensor can detect the refractive index of two samples simultaneously with a maximum sensitivity of 21300 nm/RIU. To the best of our knowledge, the sensitivity achieved in this work is the highest sensitivity with the dual sample synchronous detection sensors. Due to the simple manufacturing process, the sensor is a strong competitor for refractive index detection in the biochemical field.

Acknowledgments

Project supported by the National Natural Science Foundation of China (Grant No. 61601183 and 31671580), the Key Technologies Research and Development Program of Henan Province, China (Grant No. 202102210390 and 222102210242), and Young Backbone Teachers in University of Henan Province, China (Grant No. 2020GGJS099).

References

[1] Zhang Y J, Tian F J, Su Z L, Bai R L, Li L, Yang X H and Zhang J Z 2020 *Appl. Opt.* **59** 779
[2] Wu J J, Li S G, Liu Q and Shi M 2017 *Chin. Phys. B* **26** 114209
[3] Liu C, Yang L, Liu Q, Wang F M, Sun Z J, Sun T, Mu H W and Chu P K 2018 *Plasmonics* **13** 779
[4] Xia F, Song H, Zhao Y, Zhao W M, Wang Q, Wang X Z, Wang B T and Dai Z X 2020 *Measurement* **164** 108083
[5] Liu C, Wang J W, Wang F M, Su W Q, Yang L, Lv J W, Fu G L, Li X L, Liu Q, Sun T and Chu P K 2020 *Opt. Commun.* **464** 125496
[6] Li F, He M H, Zhang X D, Chang M and Wu Z Z 2020 *Opt. Fiber Technol.* **54** 102082
[7] Rifat A A, Ahmed R, Mahdiraji G A and Adikan F R M 2017 *IEEE Sens. J.* **17** 2776
[8] Kaur V and Singh S 2019 *Opt. Fiber Technol.* **48** 159
[9] Hossain M B, Mahendiran T V, Abdulrazak L F, Mehedi I M, Hossain M A and Rana M M 2020 *Opt. Quant. Electron.* **52** 446
[10] Guo X, Han L Y, Liu F and Li S T 2020 *Optik* **218** 164796
[11] Momota M R and Hasan M R 2018 *Opt. Mater.* **76** 287
[12] Wang H Y, Yan X, Li S G, An G W and Zhang X N 2016 *Sensors-Basel* **16** 1
[13] Wang G Y, Lu Y, Yang X C, Duan L C and Yao J Q 2019 *Appl. Opt.* **58** 5800
[14] Paul A K, Sarkar A K, Rahman A B S and Khaleque A 2018 *IEEE Sens. J.* **18** 5761
[15] Zhang Y T, Zhou C, Xia L, Yu X and Liu D M 2011 *Opt. Express* **19** 22863
[16] Abrar I, Firoz H and Rifat A A 2021 *J. Opt. Soc. Am. B* **38** 3055
[17] Azzam S I, Hameed M F O, Shehata R E A, Heikal A M and Obayya S S A 2016 *Opt. Quant. Electron.* **48** 142
[18] Yasli A, Ademgil H, Haxha S and Aggoun A 2020 *IEEE Photon. J.* **12** 1
[19] Bing P B, Sui J L, Wu G F, Guo X Y, Li Z Y, Tan L and Yao J Q 2020 *Plasmonics* **15** 1071
[20] Lu M D, Peng W, Liu Q, Liu Y and Li L X 2017 *Opt. Express* **25** 8563
[21] Lv Z G and Teng H 2021 *Chin. Phys. B* **30** 044209
[22] Kaur V and Singh S 2019 *J. Comput. Electron.* **18** 319
[23] Zhang Y X, Yuan J H and Qu Y W 2020 *Chin. Phys. B* **29** 034208
[24] Wang F M, Sun Z J, Sun T, Liu C and Bao L Y 2018 *J. Opt.* **47** 288
[25] Liu B L, Lu Y, Yang X C and Yao J Q 2016 *Opt. Eng.* **55** 117104
[26] Fan Z K, Fang S B, Li S G and Wei Z Y 2019 *Chin. Phys. B* **28** 094209
[27] Gangwar R K and Singh V K 2017 *Plasmonics* **12** 1367
[28] Hasan M R, Akter S, Rifat A A, Rana S, Ahmed K and Ahmed R 2017 *IEEE Sens. J.* **18** 133
[29] Bing P B, Wu G F, Sui J L, Zhang H T, Tan L, Li Z Y and Yao J Q 2020 *Optik* **224** 165522
[30] Liu C, Su W Q, Wang F M, Li X L, Yang L, Sun T, Mu H W and Chu P K 2019 *J. Mod. Opt.* **66** 1
[31] Al Mahfuz M, Hossain M A, Haque E, Hai N H, Namihira Y and Ahmed F 2020 *IEEE Sens. J.* **20** 7692
[32] Lou J B, Cheng T L and Li S G 2019 *Opt. Fiber Technol.* **48** 110